Title

High-Frequency Fluctuations in Antarctic Bottom Water Transport Driven by Southern Ocean Winds

Journal
Geophysical Research Letters, 48(17)

ISSN
0094-8276

Authors
Stewart, Andrew L
Chi, Xiaoyang
Solodoch, Aviv
et al.

Publication Date
2021-09-08

DOI
10.1029/2021gl094569

High-frequency fluctuations in Antarctic Bottom Water transport driven by Southern Ocean winds

Andrew L. Stewart[1], Xiaoyang Chi[1], Aviv Solodoch[1] and Andrew McC. Hogg[2]

[1]Department of Atmospheric and Oceanic Sciences, University of California, Los Angeles, California, USA
[2]Research School of Earth Sciences & Australian Research Council Centre of Excellence for Climate Extremes, Australian National University, Canberra, Australia

Key Points:

- Variations in Southern Ocean winds drive large fluctuations in northward flow of Antarctic Bottom Water (AABW) in an ocean state estimate
- AABW fluctuations are driven directly by topographic form stress, which responds to wind fluctuations over a time scale of a few days
- Over multi-year time scales, interfacial form stress adjusts to wind fluctuations, suppressing fluctuations in AABW transport

Corresponding author: Andrew L. Stewart, `astewart@atmos.ucla.edu`

Abstract

Northward flow of Antarctic Bottom Water (AABW) across the Southern Ocean comprises a key component of the global overturning circulation. Yet AABW transport remains poorly constrained by observations and state estimates, and there is presently no means of directly monitoring any component of the Southern Ocean overturning. However, AABW flow is dynamically linked to Southern Ocean surface circulation via the zonal momentum balance, offering potential routes to indirect monitoring of the transport. Exploiting this dynamical link, this study shows that wind stress fluctuations drive large AABW transport fluctuations on time scales shorter than ∼2 years, which comprise almost all of the transport variance. This connection occurs due to differing time scales on which topographic and interfacial form stresses respond to wind variability, likely associated with differences in barotropic vs. baroclinic Rossby wave propagation. These findings imply that AABW transport variability can largely be reconstructed from the surface wind stress alone.

Plain Language Summary

Antarctic Bottom Water (AABW) is the densest major body of water in the world ocean, flowing out from Antarctica and filling over 1/3 of the global subsurface. AABW has several key functions in the climate system, particularly for climate variability over centuries to millennia. However, current observing and simulation technologies produce a wide range of estimates of the rate at which AABW is injected into the global ocean. This study shows that the rate at which AABW flows northward across the Southern Ocean can be indirectly inferred, and thus monitored, from knowledge of the forces applied by winds to the ocean surface, which are more accurately estimated by current observing and simulation technologies. These wind forces produce relatively large fluctuations of AABW flow in the Southern Ocean on time scales shorter than approximately 2 years. Future measurements of AABW flow across the Southern Ocean must be made at sufficiently high frequency to resolve these fluctuations in order to avoid distortions.

1 Introduction

The formation and northward export of Antarctic Bottom Water (AABW) supplies the deepest branch of the global meridional overturning circulation (MOC) (Lumpkin & Speer, 2007; Talley, 2013). This export ventilates the global abyss, with AABW comprising over 1/3 of the volume of the sub-surface ocean (Gebbie & Huybers, 2011). In addition to supplying oxygen (Orsi et al., 2001; Gordon, 2009), AABW serves as a reservoir of carbon dioxide many times larger than the atmosphere's (Russell et al., 2006; Skinner et al., 2010). The spread of AABW is therefore arguably the most climatically important branch of the MOC on centennial to millennial timescales (Marshall & Speer, 2012).

Despite the global importance of AABW export, there are currently no direct measurements of its total meridional transport in the Southern Ocean. In contrast, deep ocean transports in the Atlantic basin are sampled by the RAPID (Johns et al., 2011), OSNAP (Schiermeier, 2013) and SAMBA (Ansorge et al., 2014) arrays, with additional arrays in preparation (Frajka-Williams et al., 2019). Estimates of AABW transport have been derived from inverse model calculations, but the available measurements permit only the multi-decadal mean transports to be estimated (Sloyan & Rintoul, 2001; Lumpkin & Speer, 2007; Naveira Garabato et al., 2016). While multi-decadal changes in the properties and transport of AABW have been inferred from hydrographic measurements (Purkey & Johnson, 2010, 2012, 2013), there remain insufficient direct measurements to monitor variability in AABW export.

While the vastness of the Southern Ocean hinders direct measurements of AABW transport, the unique dynamics of the Antarctic Circumpolar Current (ACC) might allow the transport to be inferred indirectly (Stewart & Hogg, 2017). Specifically, in the absence of zonal continental boundaries, the ACC must establish pressure gradients, and thus geostrophic flows, at the sea floor in order to balance the inputs of momentum and vorticity by the wind (Munk & Palmén, 1951; Rintoul et al., 2001). Consequently the ACC is strongly steered by major bathymetric features along its path (Hughes & De Cuevas, 2001; Hughes, 2005), around which it forms "standing meanders" (A. F. Thompson & Naveira Garabato, 2014). The export of AABW across the ACC also occurs adjacent to these bathymetric features in a series of abyssal boundary currents (Fukamachi et al., 2010; Purkey et al., 2017), establishing a direct connection between the two circulations.

The connection between AABW transport and ACC circulation is made explicit via the isopycnal zonal momentum balance (Mazloff et al., 2013), which is sketched in Fig. 1(a). Surface momentum input by the wind stress (WS) is primarily extracted from the ocean via topographic form stress (TFS) (Munk & Palmén, 1951; Masich et al., 2015). In the interior, zonal momentum is transferred downward through successively denser isopycnal layers via interfacial form stress (IFS) (Ward & Hogg, 2011; Masich et al., 2018). These form stresses support the northward flow of AABW, which induces a westward Coriolis force and thus requires a net eastward force due to the form stresses in order to satisfy geostrophic balance (Howard et al., 2015; Stewart & Hogg, 2017).

In this study we use this isopycnal momentum balance to identify a dynamical connection between high-frequency wind fluctuations (occurring over periods shorter than a few years) and variability in the northward flow of AABW. We hypothesize that such a connection should exist due to the vast difference in the time scales associated with the establishment of IFS vs. TFS, which are set by the propagation time scales of baroclinic and barotropic Rossby waves, respectively (Ward & Hogg, 2011). We use a dynamically self-consistent ocean state estimate to examine the relationships between WS, IFS, TFS and the northward flow of AABW over a range of different time scales (see Sec. 2). A key finding is that AABW transport closely tracks variations in the WS over time scales longer than a few days and shorter than a few years, which may allow a large fraction of the AABW transport variability to be reconstructed dynamically from the WS (see Sec. 3). This finding has implications for direct estimates of the abyssal overturning circulation in the Southern Ocean, and offers a potential approach to indirectly inferring the strength of this circulation (see Sec. 4).

2 Isopycnal overturning in the ECCOV4r4 global ocean state estimate

We diagnose overturning circulation variability in the Estimating the Climate and Circulation of the Ocean state estimate, Version 4, Release 4 (ECCOV4r4) (Forget et al., 2015; Fukumori et al., 2021). This product estimates the global ocean and sea ice state from 1992 to 2017 on an approximately 1° horizontal grid with 50 vertical levels. ECCO simulates the ocean and sea ice state using the MIT general circulation model (Marshall, Adcroft, et al., 1997; Marshall, Hill, et al., 1997), constrained by a range of *in situ* and remote measurements. ECCOV4r4 carries two key advantages for this study: First, the estimated ocean state is dynamically self-consistent, *i.e.* no spurious nudging of the ocean state toward observations occurs during the model integration. Second, the model state is provided as daily averages, allowing variability in the ocean state and circulation to be quantified over a wide range of time scales. This range of time scales is necessary to capture the adjustment of the ACC momentum balance to changes in wind forcing, as shown in Sec. 3.

We compute the overturning circulation using potential density referenced to 2000 db (σ_2) as the vertical coordinate, as this has been shown to more accurately capture Southern Ocean transport pathways than averaging in geopotential coordinates (Döös & Webb,

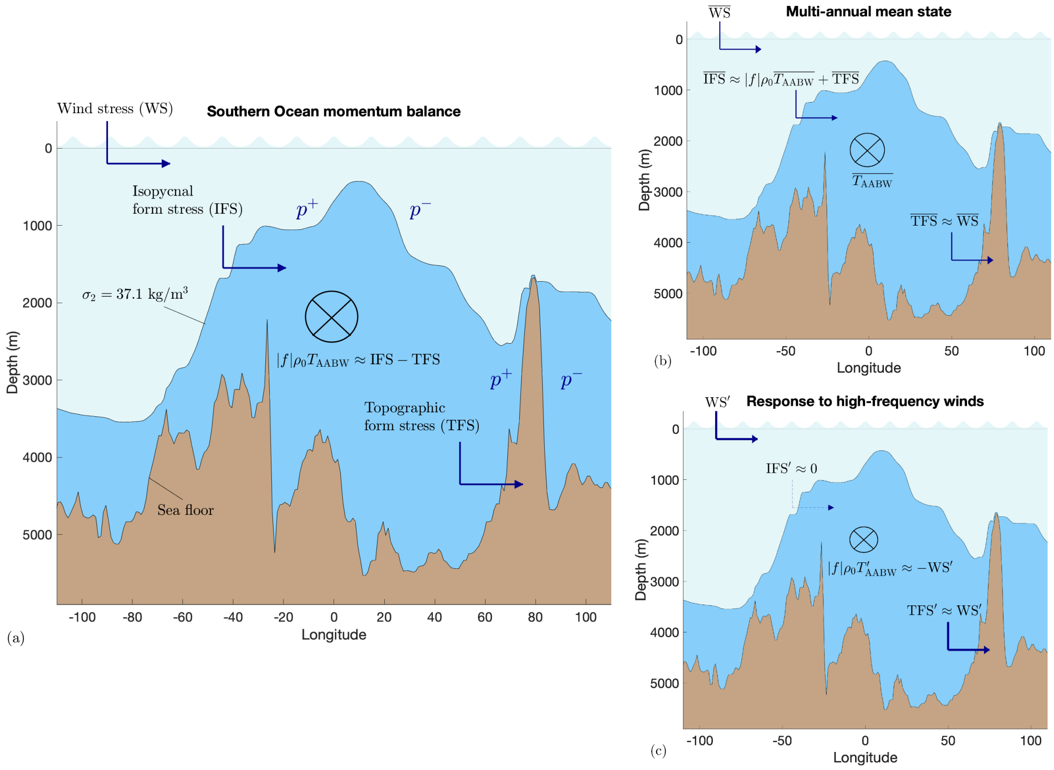

Figure 1. (a) Schematic of the Southern Ocean's zonal momentum balance and its relationship with northward flow of Antarctic Bottom Water (T_{AABW}). The brown shaded area corresponds to a section of the ECCOV4r4 bathymetry along 58°S, while the dark blue shaded area corresponds to the upper boundary of the AABW layer (defined as $\sigma_2 = 37.1\,\mathrm{kg/m^3}$ in our analysis) along the same latitude circle. The wind stress (WS) imparts zonal momentum upon the ocean surface layer, which is extracted by topographic form stress (TFS) at the sea floor. Interfacial form stress (IFS) at each isopycnal interface acts to transfer zonal momentum downward. The northward flow of AABW is approximately geostrophic, and is therefore in balance with the form stress convergence, *i.e.* IFS−TFS. (b) In a multi-annual average, the mean TFS balances the WS. Meanwhile, the IFS must exceed TFS in order to support the mean northward flow of AABW across the Southern Ocean. (c) Response to WS fluctuations over short periods (from days to several years). The TFS adjusts to changes in WS over a period of a few days, whereas IFS requires several years. Thus, high-frequency wind fluctuations translate directly to fluctuations in form stress convergence in the AABW layer, with commensurate fluctuations in the northward transport of AABW.

1994; Cessi, 2019). Specifically, we define the overturning streamfunction ψ as

$$\psi(\phi, \sigma_2, t) = \oint \int_{z=\eta_\sigma}^{z=0} v(x, \phi, z, t)\,\mathrm{d}z\mathrm{d}x, \tag{1}$$

where x denotes zonal distance, ϕ denotes latitude, z denotes elevation, t denotes time, and η_σ denotes the elevation of each σ_2 surface. Here the meridional velocity $v = v_r + v_e$ is the sum of the resolved flow, v_r, plus the parameterized eddy-induced transport, v_e (Gent & McWilliams, 1990). Thus, the overturning streamfunction can correspondingly be written as a sum of resolved plus eddy-induced components, $\psi = \psi_r + \psi_e$ (Marshall & Radko, 2003), which are discussed further in the Supporting Information.

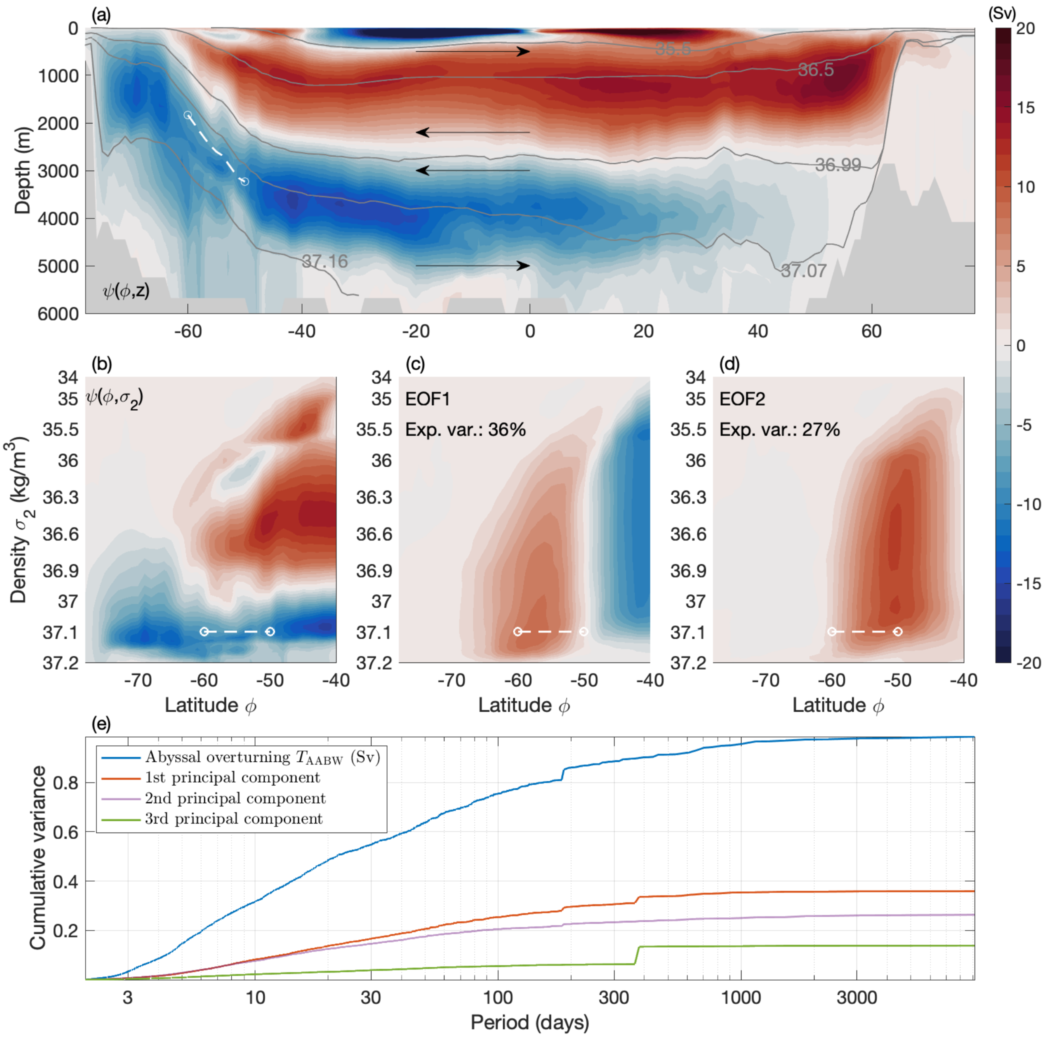

Figure 2. Isopycnal overturning circulation in the ECCOV4r4 global ocean state estimate (Forget et al., 2015), and its variability in the Southern Ocean. (a) Overturning streamfunction $\overline{\psi}$, averaged over 1992–2017 and remapped to latitude/depth space as described in Section 2. The circulation follows streamlines in the directions indicated by the black arrows. Gray contours show potential density surfaces ($\sigma_2 = 35.5, 36.5, 36.99, 37.07$ and 37.16 kg/m^3) that are approximately aligned with the boundaries and cores of the upper and lower overturning cells in the subtropics. (b) Southern Ocean overturning streamfunction ψ in latitude/density space. (c,d) First two empirical orthogonal functions (EOFs) of ψ, computed using daily variations ψ from 1992 to 2017 between 40°S and 80°S. In panels (a–d) the white dashed line indicates the isopycnal ($\sigma_2 = 37.1\,\text{kg/m}^3$) and latitude range (50–60°S) that we use to define the northward transport of Antarctic Bottom Water, T_{AABW}. (e) Cumulative variance in spectral space of T_{AABW}, and of the first three principal components of ψ.

Fig. 2(a) shows the time-averaged global overturning streamfunction, remapped to geopotential coordinates via the zonal/vertical cross-sectional areas above each isopycnal and geopotential surface (Nurser & Lee, 2004; Sun et al., 2020). The overturning circulation is very similar to the previous releases of ECCO, which accurately captures the strength of the upper branch of the circulation. The strength of the abyssal (AABW-driven) branch varies substantially among previous observationally-constrained estimates, with ECCOV4r4 lying toward the low end of this range (Cessi, 2019).

Figs. 2(b–d) show the time-averaged streamfunction and its principal modes of variability in the Southern Ocean, the latter being quantified via the first two Empirical Orthogonal Functions (EOFs) south of 40°S (Weare & Nasstrom, 1982). The EOFs reveal that variability in the streamfunction has a structure that occupies the full water column depth, with transports concentrated in the surface and bottom density classes. This structure indicates that fluctuations in meridional Ekman transport are balanced by approximately isopycnal return flows in the deepest density classes, suggesting the variability in wind stress is associated with variability in isopycnal transport of AABW. Furthermore, the magnitudes of the EOFs demonstrate that this variability in the overturning circulation is comparable in magnitude to its mean strength (the corresponding Principal Components (PCs) have each been normalized to have standard deviations of 1).

We quantify variability in meridional transport of AABW via

$$T_{\mathrm{AABW}}(t) = \left\langle \psi|_{\sigma_2=37.1\,\mathrm{kg\,m^{-3}}} \right\rangle, \tag{2}$$

where $\langle \bullet \rangle$ denotes an average from 60°S to 50°S. The $\sigma_2 = 37.1\,\mathrm{kg\,m^{-3}}$ density surface approximately tracks the maximum of the zonally-integrated abyssal overturning streamfunction in the Southern Ocean; this density surface and the meridional averaging window are indicated in Figs. 2(a–d)). In Fig. 2(e) we quantify the variability in T_{AABW} and the first two principal components of the Southern Ocean streamfunction via the cumulative spectral variance. The variability in all of these time series is strongly skewed toward high frequencies, with approximately 90% of the variance occuring on periods shorter than 1 year.

As discussed in Sec. 1, meridional transport of AABW is closely tied to the zonal momentum balance (see Fig. 1(a)). We quantify the zonally-integrated wind stress as

$$\mathrm{WS}(\phi, t) = \oint \tau^{(x)}\,\mathrm{d}x, \tag{3}$$

where $\tau^{(x)}$ denotes the zonal component of the ocean surface stress reported by ECCOV4r4. The interfacial form stress across each σ_2 surface is

$$\mathrm{IFS}(\phi, \sigma_2, t) = \oint p|_{z=\eta_\sigma} \frac{\partial \eta_\sigma}{\partial x}\,\mathrm{d}x, \tag{4}$$

where p is the pressure, and the topographic form stress is

$$\mathrm{TFS}(\phi, t) = \oint p|_{z=\eta_b} \frac{\partial \eta_b}{\partial x}\,\mathrm{d}x, \tag{5}$$

where η_b is the elevation of the ocean bottom. Like the overturning streamfunction, the IFS has both resolved (RIFS) and eddy (EIFS) components, with IFS = RIFS+EIFS. We compute the RIFS and the TFS following Masich et al. (2015, 2018) and Stewart and Hogg (2017), while (EIFS) is inferred from the eddy-induced overturning streamfunction (Gent et al., 1995), as discussed in the Supporting Information.

In isopycnal coordinates, the geostrophic relation implies that the northward flow in isopycnal layers is proportional to the form stress divergence (Mazloff et al., 2013). Over the entire AABW layer, this implies

$$|f|\rho_0 T_{\mathrm{AABW}} = \mathrm{IFS}_{\mathrm{AABW}} - \langle \mathrm{TFS} \rangle\,. \tag{6}$$

Here f is the Coriolis parameter, $\rho_0 = 1029\,\mathrm{kg\,m^{-3}}$ is the reference density, and we define $\mathrm{IFS}_{\mathrm{AABW}}$ as the interfacial form stress at the top of the AABW layer,

$$\mathrm{IFS}_{\mathrm{AABW}}(t) = \left\langle \mathrm{IFS}|_{\sigma_2=37.1\,\mathrm{kg\,m^{-3}}} \right\rangle. \tag{7}$$

In Sec. 3 (see Fig. 3(b)) and the Supporting Information we verify that Eqn. (6) holds to a very close approximation, despite the resolved components of T_{AABW} and IFS being calculated independently of one another.

3 Time scales of AABW transport response to wind fluctuations

We now examine the relationship between wind stress and AABW transport in the Southern Ocean, and link these relationships to interfacial and topographic form stresses. In Figs. 3 we quantify these relationships over a range of different time scales by applying running averages of various window lengths to $\langle\mathrm{WS}\rangle$, T_{AABW}, $\mathrm{IFS}_{\mathrm{AABW}}$ and $\langle\mathrm{TFS}\rangle$. Note that the variance in these times series occurs primarily at high frequencies (see Fig. 2(e)), so applying a smoothing window of a given width Δt tends to emphasize variability with periods close to Δt.

Fig. 3(a) shows that $\langle\mathrm{TFS}\rangle$ is strongly correlated with surface winds at all time scales, with correlation coefficient r rising from $\sim$0.73 for a smoothing window of 1 day to $r \approx 1$ for smoothing windows longer than 30 days. This indicates that the ACC approaches a balance between zonal wind stress and TFS on time scales shorter than 1 month, as is expected in equilibrium conditions (Munk & Palmén, 1951; Masich et al., 2015). In contrast, IFS is very weakly correlated with the wind variability, with $\langle\mathrm{WS}\rangle$ typically explaining just 10–20% of the variance in $\mathrm{IFS}_{\mathrm{AABW}}$. This result is consistent with our hypothesis that IFS responds to wind stress variability on a longer, multi-annual time scale than TFS.

The muted response of $\mathrm{IFS}_{\mathrm{AABW}}$ to wind variability suggests that wind-driven fluctuations of $\langle\mathrm{TFS}\rangle$ should produce corresponding fluctuations of T_{AABW}, via (6):

$$|f|\rho_0 T'_{\mathrm{AABW}} \approx -\,\langle\mathrm{TFS}\rangle' \approx -\,\langle\mathrm{WS}\rangle'\,. \tag{8}$$

Here primes $'$ denote deviations from an average over the entire ECCOV4r4 integration period. Figs. 3(a) and (b) support this relationship: T_{AABW} exhibits a correlation of $\sim$0.7 with both $\langle\mathrm{TFS}\rangle$ and $\langle\mathrm{WS}\rangle$ at 1-day smoothing, rising to $\sim$0.85 at for a smoothing window of one year. Fig. 3(b) also shows that Eqn. (6) holds ($r \gtrsim 0.9$) for all smoothing windows, verifying that fluctuations in the northward flow of AABW are indeed geostrophic, whereas T_{AABW} is essentially uncorrelated with $\mathrm{IFS}_{\mathrm{AABW}}$ on time scales shorter than $\sim$3 years. However, on longer time scales T_{AABW} becomes uncorrelated with the TFS, and exhibits a strong correlation with $\mathrm{IFS}_{\mathrm{AABW}}$, rising to a maximum of $r \approx 0.87$ for a smoothing time scale of approximately 10 years. This implies that multi-annual geostrophic AABW transport fluctuations are supported primarily by adjustments of the IFS.

A further implication of Eqn. (8) is that it should be possible to reconstruct AABW transport variability solely from knowledge of the surface wind stress. In Fig. 3(c) we illustrate this reconstruction over the entire ECCOV4r4 state estimate, with a 30-day running-average smoothing applied to both the diagnosed and reconstructed T'_{AABW}. The Nash–Sutcliffe Efficiency (McCuen et al., 2006) of this reconstruction is 0.61.

Above, we posit that the strong relationship between AABW meridional transport and zonal wind stress results from IFS and TFS responding to wind stress changes over widely differing time scales. To quantify these time scales, we use Climate Response Functions (CRFs) (Kostov et al., 2017; Hasselmann et al., 1993). Briefly, each CRF is computed by assuming that a time series, *e.g.*, $T_{\mathrm{AABW}}(t)$, is linearly related to the past history of $\langle\mathrm{WS}\rangle(t)$,

$$\rho_0|f|T_{\mathrm{AABW}}(t) = \int_0^{\tau_{\max}} \mathrm{d}\tau\; G(\tau)\cdot\langle\mathrm{WS}\rangle(t-\tau) + \varepsilon. \tag{9}$$

Here $G(\tau)$ is a Green's function and ε denotes the error in this relation. We include the factor of $\rho_0|f|$ so that the Green's function has units of s^{-1}; this factor is not needed when

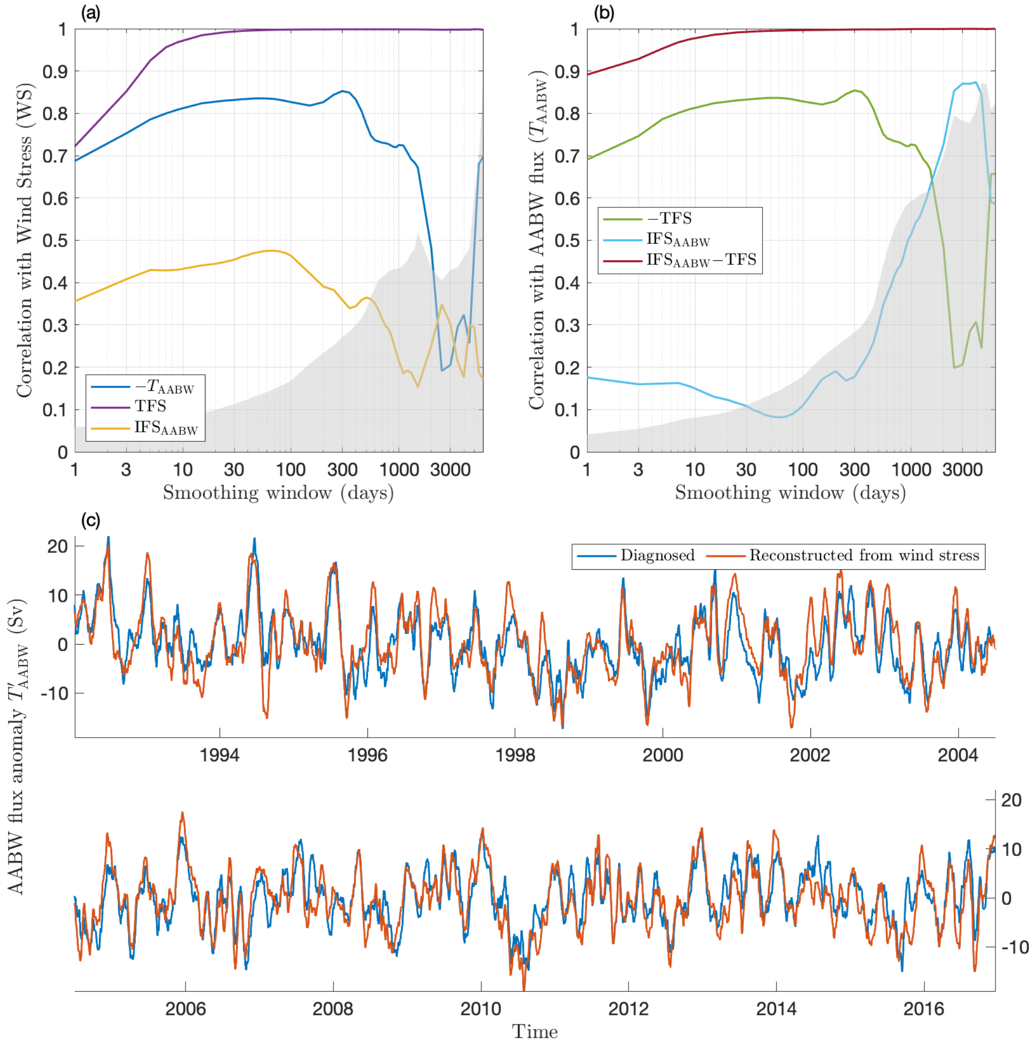

Figure 3. Time scales of the relationships between surface wind stress (WS), northward flow of AABW (T_{AABW}), interfacial form stress at the top of the AABW layer ($\mathrm{IFS}_{\mathrm{AABW}}$), and topographic form stresses (TFS). All quantities are first averaged between 50°S and 60°S, and are then smoothed via a running average with varying temporal window lengths. (a) Correlations of T_{AABW}, TFS and $\mathrm{IFS}_{\mathrm{AABW}}$ with WS, quantified via Pearson's correlation coefficient, r. (b) Correlations of TFS, IFS and IFS−TFS with T_{AABW}. In both panels (a) and (b) correlation coefficients above the gray shaded region are statistically significant ($p < 0.05$). The statistical significance threshold depends on the effective number of degrees of freedom in the smoothed time series, which we estimate via the time scale over which the autocorrelation function decays by a factor of e. (c) Time series of northward AABW transport anomalies, T'_{AABW}, as diagnosed directly from the ECCOV4r4 product and reconstructed from the surface wind stress via $\rho_0|f|T'_{\mathrm{AABW}} \approx -\mathrm{WS}'$. Both the diagnosed and reconstructed transports have been smoothed via running 30-day averages.

computing CRFs for the TFS or IFS. The normalized response to a step change in $\langle \mathrm{WS} \rangle$

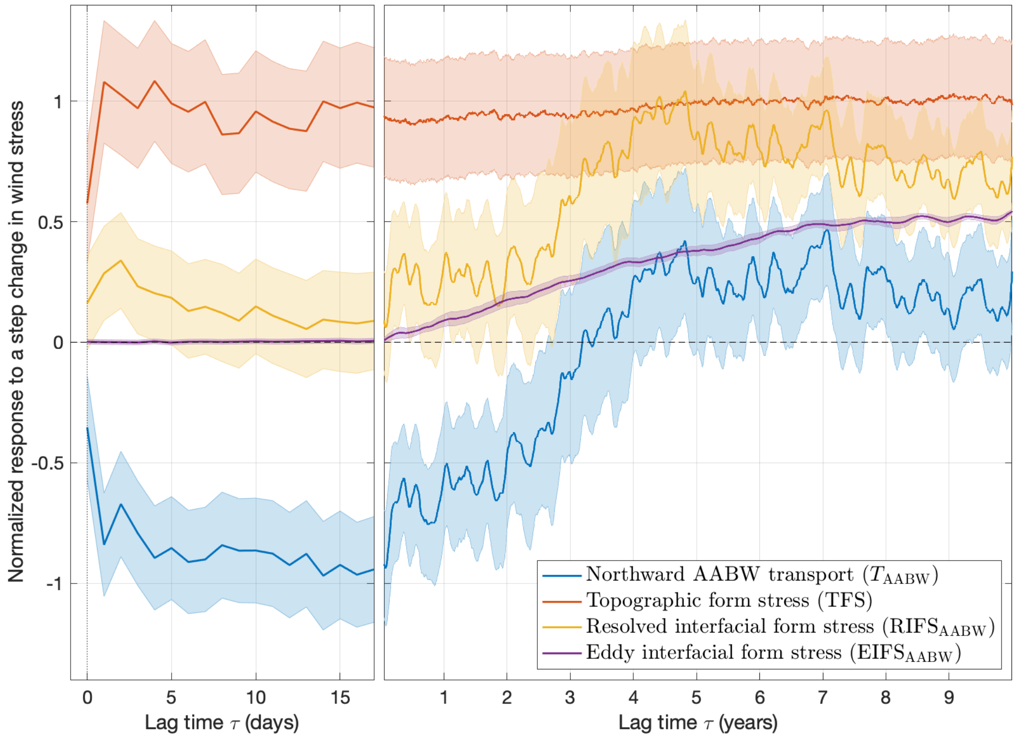

Figure 4. Response of the northward transport of AABW (T_{AABW}), topographic form stress, and interfacial form stress at the top of the AABW layer to a step-change in wind stress, diagnosed via Climate Response Functions (Hasselmann et al., 1993; Kostov et al., 2017). Shaded areas indicate one-standard deviation error bars (see Supporting Information). In the right-hand panel a 30-day running average has been applied to each of the time series. Note that combining the CRFs according to Eqn. (6), *i.e.* $\widetilde{T}_{\mathrm{AABW}} - \widetilde{\mathrm{RIFS}}_{\mathrm{AABW}} - \widetilde{\mathrm{EIFS}}_{\mathrm{AABW}} + \widetilde{\mathrm{TFS}}$, yields a sum that is very close to zero (omitted from this figure for clarity).

(occuring at a time denoted as $\tau = 0$), $\widetilde{T}_{\mathrm{AABW}}(\tau)$, may then be reconstructed as

$$\widetilde{T}_{\mathrm{AABW}}(\tau) = \int_0^{\tau} \mathrm{d}\tau^{\dagger}\; G(\tau^{\dagger}). \tag{10}$$

where $\tau^{\dagger}$ is a dummy variable of integration. Further information on this calculation, including the discretization and error estimation procedure, are provided in the Supporting Information.

Fig. 4 shows the diagnosed responses of $\rho_0|f|T_{\mathrm{AABW}}$, $\langle\mathrm{TFS}\rangle$, $\mathrm{RIFS_{AABW}}$ and $\mathrm{EIFS_{AABW}}$ to a step change in wind stress. The TFS responds almost immediately: after just 1 day the TFS has adjusted to balance the change in wind stress. In contrast, resolved (RIFS) and eddy (EIFS) components of the IFS do not change substantially for several years, with their sum ($\mathrm{IFS} = \mathrm{RIFS} + \mathrm{EIFS}$) balancing the wind stress from approximately 3 years onward. While the EIFS adjusts steadily to the step change in wind over several years, the IFS appears to undergo a relatively rapid adjustment between $\tau \approx 2\,\mathrm{yr}$ and $\tau \approx 3\,\mathrm{yr}$. The resulting change in downward momentum transfer is approximately equally distributed between RIFS and EIFS, with $\widetilde{\mathrm{RIFS}}_{\mathrm{AABW}} \approx 0.6$ and $\widetilde{\mathrm{EIFS}}_{\mathrm{AABW}} \approx 0.5$ at $\tau = 10\,\mathrm{yr}$. Consistent with the isopycnal geostrophic balance (Eqn. (6)), the slow adjustment of the IFS results in an almost immediate adjustment of T_{AABW} to a step change in wind ($\widetilde{T}_{\text{AABW}} \approx -1$ for $\tau \lesssim 30\,\text{days}$). This response persists for a few years ($\widetilde{T}_{\text{AABW}} \lesssim -0.5$ for $\tau \lesssim 2\,\text{yr}$), before decaying toward zero between $\tau = 2\,\text{yr}$ and $\tau = 3\,\text{yr}$. For $\tau \gtrsim 4\,\text{yr}$, $\widetilde{T}_{\text{AABW}}$ actually reverses sign, suggesting some over-compensation due to the adjustment of the IFS. However, it is not clear whether this transport anomaly is statistically distinguishable from zero, based on the error bars in Fig. 4.

Our correlation analysis (Fig. 3) and CRFs (Fig. 4) indicate that IFS responds to changes in wind stress on a much slower time scale (2–3 years) than TFS does (∼1 day). A possible dynamical interpretation of this difference is that the barotropic and baroclinic responses are governed by the propagation speeds of barotropic and baroclinic Rossby waves, which differ by 2–3 orders of magnitude (Anderson & Gill, 1975; Ward & Hogg, 2011). However, our results do not provide an explicit link to planetary wave dynamics, so we leave a specific investigation of the underlying dynamical mechanism for further study. We additionally note that these dynamics do not appear to be unique to the ACC core latitudes (60°S–50°S): similarly strong correlations between the surface wind stress and AABW transport are found throughout the Southern Ocean (latitudes south of 30°S, see Supporting Information).

4 Discussion and conclusions

The major finding of this study is that fluctuations in Southern Ocean winds drive variability in meridional transport of AABW over time scales shorter than approximately 2 years (Figs. 3(a) and 4). Fluctuations on these time scales account for almost all of the variability in the winds (Hell et al., 2021) and the export of AABW (Fig. 2(e)). Furthermore, the transport fluctuations are comparable to the mean meridional transport of AABW (Fig. 3(c)).

The mechanism underlying this relationship is summarized schematically in Figs. 1(b) and (c). Over longer time scales (≳3 years), our findings reproduce the momentum balance of the Southern Ocean that has previously been reported under equilibrium conditions (Munk & Palmén, 1951; Masich et al., 2015). The surface wind stress is transferred down to the sea floor by IFS and then removed by TFS, as shown in Fig. 4 and illustrated in Fig. 1(b). Northward flow of AABW occurs in the deepest density classes, and geostrophic balance (Eqn. (6)) requires that the IFS exceed the magnitude of the TFS to support this flow (see Fig. 3(b) and Supporting Information Fig. S1). On shorter time scales (≲2 years), TFS continues to adjust to wind stress fluctuations, whereas IFS remains approximately constant (Fig. 1(c)). Thus, the fluctuating TFS induces AABW transport variations that are approximately equal and opposite to the wind-driven surface Ekman transport fluctuations (Eqn. (8)). These findings are qualitatively consistent with the differing time scales of barotropic vs. baroclinic respones due to the associated Rossby wave propagation speeds (Anderson & Gill, 1975; Ward & Hogg, 2011). On very short time scales (≲15 days) the relationship between wind stress, TFS and AABW transport weakens slightly (Figs. 3 and 4), likely associated with the time scale of the ACC's barotropic response to wind stress variability.

A caveat to these findings is that the abyssal overturning circulation in ECCOV4r4 is less well constrained than, *e.g.*, the upper branch of the global overturning circulation (Cessi, 2019). However, the dynamical self-consistency of ECCOV4r4 gives us confidence that the mechanism underlying the high-frequency wind-driven fluctuations in AABW export is faithfully simulated in this product. Another caveat is that ECCOV4r4 parameterizes the effects of mesoscale eddies, which might otherwise be expected to introduce additional AABW transport variability. This effect could potentially weaken the wind/AABW relationship on sub-annual time scales, although substantial cancellation of eddy-induced flows may be anticipated in a circumpolar integral. It is also unclear whether parameterized eddies accurately capture the time scale over which eddy IFS adjusts to winds (see Fig. 4), though we note that previous eddy-resolving model studies have found that the Southern Ocean eddies adjust to wind changes over a time scale of several years (Sinha & Abernathey, 2016). Repetition of our analysis in a model that permits or resolves mesoscale eddies may be necessary to address the contribution of eddies to AABW transport variability.

A key implication of our findings is that Southern Ocean abyssal overturning circulation variability may be at least partially monitored using surface zonal wind stress, which in turn might be inferred from reanalysis products or the Southern Annular Mode index (D. W. J. Thompson & Wallace, 2000). This study therefore contributes to ongoing efforts to find methods of indirectly inferring global overturning circulation variability (Frajka-Williams et al., 2019). Such efforts have thus far primarily focused on the Atlantic, though winds have been shown to drive deep-reaching overturning circulation variability in both the Atlantic and Indo-Pacific basins (Tandon et al., 2020). However, inference of AABW transport from wind fluctuations excludes longer-term variability, *e.g.* associated with variations in source water export and properties (Abrahamsen et al., 2019; Silvano et al., 2020). The relatively large wind-driven fluctuations in AABW transport may also explain the pronounced variability observed in direct measurements of AABW velocities (Fukamachi et al., 2010), though its contribution relative to mesoscale variability remains to be evaluated. Future observations of AABW transport in the Southern Ocean should account for these high-frequency fluctuations so as to avoid aliasing, for example in inferences of transport trends.

Acknowledgments

This material is based in part upon work supported by the National Science Foundation under Grant Number OPP-2023244, and by the National Aeronautics and Space Administration ROSES Physical Oceanography program under grant number 80NSSC19K1192. The ECCOV4r4 state estimate data used in this study is publicly available from NASA's online repositories: https://data.nas.nasa.gov/ecco/. The MATLAB codes that were used to analyze the ECCOV4r4 data and create the plots presented in this study are available at https://doi.org/10.5281/zenodo.4815573. The analysis in this study made use of various MATLAB toolboxes: gcmfaces (https://doi.org/10.5281/zenodo.3606908), the Climate Data Toolbox (CDT, https://doi.org/10.5281/zenodo.2590731) and cmocean (Thyng et al., 2016). Without implying endorsement, the authors thank Andrew Thompson for useful discussions related to this study. The authors thank two anonymous reviewers for constructive suggestions that improved the submitted manuscript.

References

Abrahamsen, E. P., Meijers, A. J. S., Polzin, K. L., Naveira Garabato, A. C., King, B. A., Firing, Y. L., … Meredith, M. P. (2019). Stabilization of dense Antarctic water supply to the Atlantic Ocean overturning circulation. *Nat. Clim. Change*, *9*(10), 742–746.

Anderson, D. L. T., & Gill, A. E. (1975). Spin-up of a stratified ocean, with applications to upwelling. In *Deep sea res.* (Vol. 22, pp. 583–596).

Ansorge, I. J., Baringer, M. O., Campos, E. J. D., Dong, S., Fine, R. A., Garzoli, S. L., … others (2014). Basin-wide oceanographic array bridges the South Atlantic. *EOS*, *95*(6), 53–54.

Cessi, P. (2019). The global overturning circulation. *Ann. Rev. Mar. Sci.*, *11*, 249–270.

Döös, K., & Webb, D. J. (1994). The Deacon cell and the other meridional cells of the Southern Ocean. *J. Phys. Oceanogr.*, *24*, 429–429.

Forget, G., Campin, J.-M., Heimbach, P., Hill, C. N., Ponte, R. M., & Wunsch, C. (2015). ECCO version 4: an integrated framework for non-linear inverse modeling and global ocean state estimation. *Geosci. Model Dev.*, *8*(10), 3071–

3104.
Frajka-Williams, E., Ansorge, I. J., Baehr, J., Bryden, H. L., Chidichimo, M. P., Cunningham, S. A., ... others (2019). Atlantic Meridional Overturning Circulation: Observed transport and variability. *Front. Mar. Sci.*, *6*, 260.
Fukamachi, Y., Rintoul, S. R., Church, J. A., Aoki, S., Sokolov, S., Rosenberg, M. A., & Wakatsuchi, M. (2010). Strong export of Antarctic Bottom Water east of the Kerguelen Plateau. *Nat. Geosci.*, *3*(5), 327–331.
Fukumori, I., Wang, O., Fenty, I., Forget, G., Heimbach, P., & Ponte, i. M. (2021, February). *Synopsis of the ECCO Central Production Global Ocean and Sea-Ice State Estimate, Version 4 Release 4.* Zenodo. Retrieved from `https://doi.org/10.5281/zenodo.4533349` doi: 10.5281/zenodo.4533349
Gebbie, G. A., & Huybers, P. (2011). How is the ocean filled? *Geophys. Res. Lett.*, *38*.
Gent, P. R., & McWilliams, J. C. (1990). Isopycnal mixing in ocean circulation models. *J. Phys. Oceanogr.*, *20*(1), 150–155.
Gent, P. R., Willebrand, J., McDougall, T. J., & McWilliams, J. C. (1995). Parameterizing eddy-induced tracer transports in ocean circulation models. *J. Phys. Oceanogr.*, *25*(4), 463–474.
Gordon, A. L. (2009). Bottom water formation. In J. H. Steele, S. A. Thorpe, & K. K. Turekian (Eds.), *Ocean currents* (pp. 263–269). Associated Press.
Hasselmann, K., Sausen, R., Maier-Reimer, E., & Voss, R. (1993). On the cold start problem in transient simulations with coupled atmosphere-ocean models. *Climate Dyn.*, *9*(2), 53–61.
Hell, M. C., Cornuelle, B. D., Gille, S. T., & Lutsko, N. J. (2021). Time-Varying Empirical Probability Densities of Southern Ocean Surface Winds: Linking the Leading Mode to SAM and Quantifying Wind Product Differences. *J. Climate*, 1–80.
Howard, E., Hogg, A. M., Waterman, S., & Marshall, D. P. (2015). The injection of zonal momentum by buoyancy forcing in a Southern Ocean model. *J. Phys. Oceanogr.*, *45*(1), 259–271.
Hughes, C. W. (2005). Nonlinear vorticity balance of the Antarctic Circumpolar Current. *J. Geophys. Res. Oceans*, *110*(C11).
Hughes, C. W., & De Cuevas, B. A. (2001). Why western boundary currents in realistic oceans are inviscid: A link between form stress and bottom pressure torques. *J. Phys. Oceanogr.*, *31*(10), 2871–2885.
Johns, W. E., Baringer, M. O., Beal, L. M., Cunningham, S. A., Kanzow, T., Bryden, H. L., ... Shaw, B. (2011). Continuous, array-based estimates of Atlantic Ocean heat transport at 26.5 N. *J. Climate*, *24*(10), 2429–2449.
Kostov, Y., Marshall, J., Hausmann, U., Armour, K. C., Ferreira, D., & Holland, M. M. (2017). Fast and slow responses of Southern Ocean sea surface temperature to SAM in coupled climate models. *Climate Dyn.*, *48*(5-6), 1595–1609.
Lumpkin, R., & Speer, K. (2007). Global ocean meridional overturning. *J. Phys. Oceanogr.*, *37*(10), 2550–2562.
Marshall, J., Adcroft, A., Hill, C., Perelman, L., & Heisey, C. (1997). A finite-volume, incompressible Navier Stokes model for studies of the ocean on parallel computers. *J. Geophys. Res. Oceans*, *102*, 5753–5766.
Marshall, J., Hill, C., Perelman, L., & Adcroft, A. (1997). Hydrostatic, quasi-hydrostatic, and nonhydrostatic ocean modeling. *J. Geophys. Res. Oceans*, *102*, 5733–5752.
Marshall, J., & Radko, T. (2003). Residual-mean solutions for the Antarctic Circumpolar Current and its associated overturning circulation. *J. Phys. Oceanogr.*, *33*(11), 2341–2354.
Marshall, J., & Speer, K. (2012). Closure of the meridional overturning circulation through Southern Ocean upwelling. *Nature Geosci.*, *5*(3), 171–180.
Masich, J., Chereskin, T. K., & Mazloff, M. R. (2015). Topographic form stress in

the Southern Ocean state estimate. *J. Geophys. Res. Oceans*, *120*(12), 7919–7933.
Masich, J., Mazloff, M. R., & Chereskin, T. K. (2018). Interfacial form stress in the Southern Ocean State Estimate. *J. Geophys. Res. Oceans*, *123*(5), 3368–3385.
Mazloff, M. R., Ferrari, R., & Schneider, T. (2013). The Force Balance of the Southern Ocean Meridional Overturning Circulation. *J. Phys. Oceanogr.*, *43*(6), 1193–1208.
McCuen, R. H., Knight, Z., & Cutter, A. G. (2006). Evaluation of the Nash–Sutcliffe efficiency index. *J. Hydro. Eng.*, *11*(6), 597–602.
Munk, W. H., & Palmén, E. (1951). Note on the dynamics of the Antarctic Circumpolar Current. *Tellus*, *3*(1), 53–55.
Naveira Garabato, A. C., Zika, J. D., Jullion, L., Brown, P. J., Holland, P. R., Meredith, M. P., & Bacon, S. (2016). The thermodynamic balance of the Weddell Gyre. *Geophys. Res. Lett.*, *43*(1), 317–325.
Nurser, A. J. G., & Lee, M. M. (2004). Isopycnal averaging at constant height. Part I: The formulation and a case study. *J. Phys. Oceanogr.*, *34*(12), 2721–2739.
Orsi, A. H., Jacobs, S. S., Gordon, A. L., & Visbeck, M. (2001). Cooling and ventilating the abyssal ocean. *Geophys. Res. Lett.*, *28*(15), 2923–2926.
Purkey, S. G., & Johnson, G. C. (2010). Warming of global abyssal and deep Southern Ocean waters between the 1990s and 2000s: Contributions to global heat and sea level rise budgets. *J. Climate*, *23*(23), 6336–6351.
Purkey, S. G., & Johnson, G. C. (2012). Global contraction of Antarctic Bottom Water between the 1980s and 2000s. *J. Climate*, *25*(17), 5830–5844.
Purkey, S. G., & Johnson, G. C. (2013). Antarctic Bottom Water Warming and Freshening: Contributions to Sea Level Rise, Ocean Freshwater Budgets, and Global Heat Gain. *J. Climate*, *26*(16), 6105–6122.
Purkey, S. G., Smethie Jr, W. M., Gebbie, G., Gordon, A. L., Sonnerup, R. E., Warner, M. J., & Bullister, J. L. (2017). A Synoptic View of the Ventilation and Circulation of Antarctic Bottom Water from Chlorofluorocarbons and Natural Tracers. *Ann. Rev. Mar. Sci.*, *10*(1), 503-527.
Rintoul, S., Hughes, C., & Olbers, D. (2001). The Antarctic Circumpolar Current System. In *Ocean circulation and climate. g. siedler, j. church and j. gould, eds. new york: Academic press. p.* (pp. 271–302).
Russell, J. L., Dixon, K. W., Gnanadesikan, A., Stouffer, R. J., & Toggweiler, J. R. (2006). The Southern Hemisphere westerlies in a warming world: Propping open the door to the deep ocean. *J. Climate*, *19*(24), 6382–6390.
Schiermeier, Q. (2013). Oceans under surveillance. *Nature*, *497*(7448), 167–168.
Silvano, A., Foppert, A., Rintoul, S. R., Holland, P. R., Tamura, T., Kimura, N., ... others (2020). Recent recovery of antarctic bottom water formation in the ross sea driven by climate anomalies. *Nat. Geosci.*, *13*(12), 780–786.
Sinha, A., & Abernathey, R. P. (2016). Time scales of Southern Ocean eddy equilibration. *J. Phys. Oceanogr.*, *46*(9), 2785–2805.
Skinner, L., Fallon, S., Waelbroeck, C., Michel, E., & Barker, S. (2010). Ventilation of the deep Southern Ocean and deglacial CO2 rise. *Science*, *328*(5982), 1147–1151.
Sloyan, B. M., & Rintoul, S. R. (2001). The Southern Ocean limb of the global deep overturning circulation. *J. Phys. Oceanogr.*, *31*(1), 143–173.
Stewart, A. L., & Hogg, A. M. (2017). Reshaping the Antarctic Circumpolar Current via Antarctic Bottom Water Export. *J. Phys. Oceanogr.*, *47*(10), 2577–2601.
Sun, S., Eisenman, I., Zanna, L., & Stewart, A. L. (2020). Surface constraints on the depth of the Atlantic meridional overturning circulation: Southern Ocean versus North Atlantic. *J. Climate*, *33*(8), 3125–3149.
Talley, L. D. (2013). Closure of the global overturning circulation through the Indian, Pacific, and Southern Oceans: Schematics and transports. *Oceanography*,

26(1), 80–97.
Tandon, N. F., Saenko, O. A., Cane, M. A., & Kushner, P. J. (2020). Interannual variability of the global meridional overturning circulation dominated by Pacific Variability. *J. Phys. Oceanogr.*, *50*(3), 559–574.
Thompson, A. F., & Naveira Garabato, A. C. (2014). Equilibration of the Antarctic Circumpolar Current by standing meanders. *J. Phys. Oceanogr.*, *44*(7), 1811–1828.
Thompson, D. W. J., & Wallace, J. M. (2000). Annular modes in the extratropical circulation. Part I: Month-to-month variability. *J. Climate*, *13*(5), 1000–1016.
Thyng, K. M., Greene, C. A., Hetland, R. D., Zimmerle, H. M., & DiMarco, S. F. (2016). True colors of oceanography: Guidelines for effective and accurate colormap selection. *Oceanogr.*, *29*(3), 9–13.
Ward, M. L., & Hogg, A. M. (2011). Establishment of momentum balance by form stress in a wind-driven channel. *Ocean Modell.*, *40*(2), 133–146.
Weare, B. C., & Nasstrom, J. S. (1982). Examples of extended empirical orthogonal function analyses. *Mon. Weather Rev.*, *110*(6), 481–485.